
Princeton Plasma Physics Laboratory

PPPL-

PPPL-



Prepared for the U.S. Department of Energy under Contract DE-AC02-09CH11466.

Princeton Plasma Physics Laboratory

Report Disclaimers

Full Legal Disclaimer

This report was prepared as an account of work sponsored by an agency of the United States Government. Neither the United States Government nor any agency thereof, nor any of their employees, nor any of their contractors, subcontractors or their employees, makes any warranty, express or implied, or assumes any legal liability or responsibility for the accuracy, completeness, or any third party's use or the results of such use of any information, apparatus, product, or process disclosed, or represents that its use would not infringe privately owned rights. Reference herein to any specific commercial product, process, or service by trade name, trademark, manufacturer, or otherwise, does not necessarily constitute or imply its endorsement, recommendation, or favoring by the United States Government or any agency thereof or its contractors or subcontractors. The views and opinions of authors expressed herein do not necessarily state or reflect those of the United States Government or any agency thereof.

Trademark Disclaimer

Reference herein to any specific commercial product, process, or service by trade name, trademark, manufacturer, or otherwise, does not necessarily constitute or imply its endorsement, recommendation, or favoring by the United States Government or any agency thereof or its contractors or subcontractors.

PPPL Report Availability

Princeton Plasma Physics Laboratory:

<http://www.pppl.gov/techreports.cfm>

Office of Scientific and Technical Information (OSTI):

<http://www.osti.gov/bridge>

Related Links:

[U.S. Department of Energy](#)

[Office of Scientific and Technical Information](#)

[Fusion Links](#)

Kinetic Neoclassical Transport in the H-mode Pedestal

D.J. Battaglia¹, K.H. Burrell², C.S. Chang¹, S. Ku¹, J.S. deGrassie², and B.A. Grierson¹

¹*Princeton Plasma Physics Laboratory, P.O. Box 451, Princeton, New Jersey, USA*

²*General Atomics, P.O. Box 85608, San Diego, California, USA*

Abstract. Multi-species kinetic neoclassical transport through the QH-mode pedestal and scrape-off layer on DIII-D is calculated using XGC0, a 5D full-f particle-in-cell drift-kinetic solver with self-consistent neutral recycling and sheath potentials. Quantitative agreement between the flux-driven simulation and the experimental electron density, impurity density and orthogonal measurements of impurity temperature and flow profiles is achieved by adding random-walk particle diffusion to the guiding-center drift motion. The radial electric field (E_r) that maintains ambipolar neoclassical transport across flux surfaces and to the wall is computed self-consistently on closed and open magnetic field lines, and is in excellent agreement with experiment. The E_r inside the separatrix is the unique solution that balances the outward flux of thermal tail deuterium ions against the outward neoclassical electron flux and inward pinch of impurity and colder deuterium ions. Particle transport in the pedestal is primarily due to anomalous transport, while the ion heat and momentum transport is primarily due to the neoclassical transport. The full-f treatment quantifies the non-Maxwellian energy distributions that describe a number of experimental observations in low-collisionality pedestals on DIII-D, including intrinsic co- I_p parallel flows in the pedestal, ion temperature anisotropy and large impurity temperatures in the scrape-off layer.

PACS Nos.:

I. INTRODUCTION

Magnetically confined high-temperature plasmas are observed to self-organize into a high-confinement or H-mode state with an edge pressure pedestal: a steep pressure gradient localized to a narrow region inside the plasma boundary. H-mode is an attractive operating regime for future fusion reactors since the pressure pedestal reduces the plasma volume required to achieve the core fusion performance, consequently reducing the size and cost of the reactor. The multi-scale self-organization of the H-mode pedestal is qualitatively understood¹; however the first-principles models necessary for its quantitative prediction and optimization is an active area of research². Rapid improvement in diagnostic resolution and computational power is quickly advancing the science necessary for understanding the non-linear multi-scale physics that establish and sustain the H-mode regime on tokamaks. This article describes the first effort to leverage petascale computational resources and high-fidelity diagnostic measurements to self-consistently quantify the role of kinetic neoclassical, anomalous and neutral transport processes in the self-organization of the H-mode pedestal. The ability of the simulation to simultaneously capture the experimentally observed density, temperature, electric field and parallel flow in the H-mode edge represents a major step toward the development of a quantitative predictive tool for optimizing the boundary plasma in nuclear fusion devices.

The reduced transport leading to the H-mode pedestal is attributed to the suppression of instabilities near the plasma boundary that normally drive large turbulent fluxes of particles, energy and momentum out of the confined plasma^{3,4}. The maximum pressure difference across the pedestal is typically limited by peeling-ballooning instabilities that

become non-linearly unstable resulting in an edge-localized mode (ELM) that explosively releases a burst of particles and energy across the pedestal region⁵. ELMs can deliver an impulsive heat load to the first wall material, and are predicted to challenge the material limits in future burning-plasma devices, such as ITER. Therefore, considerable effort in fusion research is devoted to understanding the requirements for mitigating or eliminating ELMs while achieving H-mode confinement.

One attractive solution for ELM control is the quiescent H-mode (QH-mode) regime where sufficient edge toroidal flow shear is maintained to stabilize the kink-peeling instabilities at finite amplitude such that the explosive ELM event never occurs^{6,7,8}. The saturated mode is often termed an edge harmonic oscillation (EHO) since it is observed to be multi-harmonic, although the EHO can sometimes be broadband in frequency. The EHO provides enough additional particle transport that the discharge can achieve steady-state transport where the pedestal is maintained at the kink-peeling stability limit while avoiding any detectable ELMs and preventing the accumulation of impurities.

The steady-state conditions achieved with QH-mode are well suited for studying the particle, energy and momentum transport through the pedestal in high-performance tokamak plasmas. Diagnostics can employ large time integrations to improve the statistics of measurements since the saturated transport lasts many seconds. Furthermore, the spatial resolution of measurements with fixed diagnostic chord views can be improved using gradual motions in the radial position of the plasma boundary (i.e., an edge sweep). The numerical simulations presented in this letter are compared to previously published results from Burrell et al. that employed an edge sweep to collect high-resolution measurements of the QH-mode pedestal on the DIII-D tokamak⁹.

The reduction in the turbulent transport observed in the H-mode pedestal suggests that neoclassical transport becomes important, similar to what is observed with internal transport barriers in the plasma core¹⁰. However, this hypothesis is difficult to test using analytical neoclassical theory due to the breakdown of the assumptions that are typically valid in the core plasma. Namely, kinetic, non-local and ion-neutral effects that are insignificant in the plasma core become significant in the H-mode pedestal.

Analytic neoclassical transport theory assumes that drift-orbit radial excursions of all particles are much smaller than the gradient scale lengths of the plasma. However, in the H-mode pedestal, the orbit excursions are on the same order as the gradient scale lengths, especially for trapped ions in the high-energy tail of the distribution with the largest banana widths. Therefore, a particle can experience very different plasma conditions over a full drift orbit (i.e., non-local effects). Furthermore, ion collisions with neutral particles originating from wall recycling are significant in the plasma edge and can provide sources and sinks for plasma density, energy and momentum. Finally, a valid assumption for neoclassical transport in an axisymmetric plasma core is that all drift orbits are closed and thus transport is automatically ambipolar. In other words, the ion and electron radial neoclassical currents across flux surfaces are always balanced in steady-state, regardless of the radial electric field (E_r). This assumption is not valid in the plasma edge due to thermal ion orbit loss.

The drift motions of ions in the H-mode pedestal can cross the boundary (i.e., separatrix) between the closed flux surfaces and the open field lines of the scrape-off layer (SOL). Once the ion enters the SOL, collisional and collision-less processes can result in the particle being lost on the open field lines to the material wall. Radial drift

excursions of ions are considerably larger than electrons, so this loss mechanism is non-ambipolar, meaning the ion and electron loss rates are not automatically balanced. Consequently, E_r is constrained to a specific value (i.e., root solution) that reduces ion orbit loss enough to maintain ambipolar transport of charged particles across the separatrix. Similarly, the electron parallel loss rate in the SOL along the open field lines to the wall is much larger than the ion loss rate and a sheath develops with a positive electric potential on the open field line to maintain ambipolar particle loss.

The role of ion orbit loss in driving transport, flows and E_r at the plasma edge has been considered for decades^{11,12,13,14,15}. A number of studies have demonstrated that it is fairly straightforward to compute the collisionless ion orbits for a realistic magnetic and electric field topology and generate the corresponding loss hole in velocity space due to ions striking a material limiter^{16,17,18}. These calculations provide a qualitative tool for examining the relationship between the plasma magnetic and electric field topology and the parallel flow associated with an empty loss hole¹⁹. Quantifying the impact of ion orbit loss on transport and E_r requires more comprehensive calculations that include collisions and all sources and sinks of particles, energy and momentum in order to determine the scattering rate of ions into and out of the loss hole.

The magnitude and gradient in the E_r root solution around the separatrix due to ion orbit loss and wall sheaths results in steady-state particle distributions that are non-Maxwellian and transport that is non-local. This has motivated the development of full-f particle-in-cell (PIC)²⁰ and continuum^{21,22} numerical transport simulations that do not impose any constraints on the distribution function of the particles and explicitly calculate the non-local effects. The simulations presented in this article use XGC0, a

full-f drift-kinetic multi-species (e^- , D^+ , C^{6+} , D^0 , C^0) PIC solver for a realistic magnetic geometry²³. XGC0 is a highly-parallelized code that follows the drift motion of order 10 million particles undergoing mass-energy-momentum conserving collisions with a background plasma. The plasma potential is self-consistently evolved to maintain ambipolar transport across flux surfaces and to the wall. Charged particles lost to the wall are reborn as neutrals that undergo collisions with the charged plasma species. Core transport modeling is employed to prescribe realistic energy, momentum and particle flux across the core-edge boundary of the simulation.

XGC0 aims to self-consistently simulate the physics of H-mode pedestal transport on the ion- and electron- drift orbit scale (order millimeters and milliseconds). Longer scale processes, such as the current diffusion impacting the magnetic geometry or the wall material properties impacting neutral fueling are nearly constant on this scale. Therefore, the magnetic geometry and neutral recycling rates are fixed through the entire XGC0 simulation. The short scale processes, namely turbulent transport from instabilities, are important and impact the intermediate scale addressed with XGC0. Self-consistent solutions at this scale are computed with the code XGC1^{24,25} at much larger computational expense; evolving these simulations over many heat or particle diffusion times (multi-milliseconds) is typically intractable. A planned simulation framework will employ a multi-scale coupling of XGC0 and XGC1 in order to address the relevant first-principles transport physics in an efficient calculation²⁶. As a standalone code, XGC0 contains free parameters for guiding-center random-walk motion that can be added to the particle drift-orbit motion to approximate the impact of small-scale turbulent perturbations. The free parameters of the ad-hoc random-walk model, such as the random-walk step size, are

motivated by theory, but are typically tuned to improve the match between the simulation and measurements. The result from this interpretative modeling approach provides insight into the contribution of kinetic neoclassical transport, anomalous transport and self-consistent neutral fueling physics to the overall measured transport level.

This article presents the first application of interpretative multi-species XGC0 to the transport in the H-mode pedestal for a low-collisionality deuterium plasma with a carbon impurity. Section 2 provides a detailed description of the model used in this work. The interpretive transport analysis is applied to measurements of the edge transport barrier made on the DIII-D tokamak with high spatial resolution⁹, as summarized in Section 3. It is found that the deuterium energy and momentum transport is predominately neoclassical in the steep-gradient region of the pedestal. The calculated neoclassical E_r required for ambipolar transport is in quantitative agreement with the E_r profile inferred from experiment. The simulation indicates that the ambipolar neoclassical E_r is primarily established by the balancing of deuterium ion orbit loss against an outward neoclassical flux of electrons and an inward pinch of the carbon impurity and cold deuterium ions. Kinetic effects play a significant role in the neoclassical transport and result in steady-state energy distributions that are non-Maxwellian throughout the pedestal and SOL. This explains a number of experimental observations not captured in fluid or analytical neoclassical models including ion temperature anisotropy, intrinsic parallel flows in the opposite direction of the applied torque, and large ion temperatures in the SOL. Section 4 discusses the implications of these results and Section 5 provides a conclusion and outlines future work.

2. CALCULATION OF H-MODE TRANSPORT USING THE XGC0 CODE

XGC0 is a particle-in-cell code where the solution domain is reduced from 6D to 5D by excluding the gyro-motion and following the guiding center drift motion of the particles. The simulation results presented in this paper assume axisymmetry to reduce the computational space to 4D (2D in physical space: R, Z, and 2D in velocity space: v_{\parallel}, v_{\perp}). The code is initialized by randomly distributing 3.84 million particles for each species (D^+, e^-, C^{6+}) over the solution domain assuming Maxwellian energy distributions that are described by an initial guess of the plasma properties (n, T, v) on each flux surface. The ion particle positions are advanced in time steps of 0.1 -0.2 μs with the equations of motion given in²³. The electrons are given a mass equal to 2% of a proton (mass enhancement of 36.7) such that the electron guiding centers are advanced on $\sqrt{M_i/m_e} = 10$ sub-steps for each ion step. XGC0 is a highly parallelized code, and the simulations presented in this paper used 768 processors that each tracked about 15,000 particles.

The drift motion of the guiding centers is computed using a static magnetic topology and a dynamic flux surface electrostatic potential (Φ). The poloidal cross-section of the axisymmetric magnetic topology used for the simulations presented in this paper is shown in Figure 1. Each contour represents a surface of constant poloidal flux (ψ) and the thick contour at $\psi_N = (\psi - \psi_0)/(\psi_X - \psi_0) = 0.8$ designates the inner boundary of the simulation and the limiter (thick black line) is the outer boundary. If a particle leaves the simulation domain across the inner boundary, it is moved to the approximate poloidal location where it would have reentered the simulation domain if it completed a collisionless orbit. Ion particles that cross a limiter surface are removed from the

simulation while electrons are reflected to simulate the action of a sheath. The accumulated ion charge lost from a each open flux surface in the SOL through parallel flow to the wall and perpendicular cross-field motion is evaluated after 10-50 ion steps and then a corresponding number of recently reflected electrons are removed from the domain to maintain charge balance. The highest energy reflected electrons are chosen for removal and the electrostatic potential for the flux surface is defined as the lowest energy electron lost from the flux surface (i.e. the sheath potential). This method for computing the sheath assumes currents flow resistance-free in the limiter structure since the electron and ion loss currents are not necessarily balanced at every individual wall segment. The potential is constant on each flux surface ($E_{\parallel} = 0$) and therefore the calculations do not capture the potential variation along the flux surfaces due to a sheath. The potential is fixed at zero for $\psi_N \geq 1.05$ for code stability. The potential at the inner boundary is defined such that the second derivative of the potential is zero.

The flux-surface averaged neoclassical radial ion and electron flux are evaluated after each ion time step and, if the fluxes are unbalanced, the potential on the closed flux surface is adjusted (see eq. 4 in [23]). The polarization current that offsets the net neoclassical current in a time-varying electric field is not captured in a guiding-center code and a density imbalance can develop in the calculated ion and electron guiding-center densities. The simulation is initialized with a neoclassical E_r that is close to the final answer so that the final difference between the electron and ion guiding-center charge density inside the separatrix (i.e. the polarization density) is minimal.

The guiding-center solution tends to produce a discontinuous E_r ($\sim d\Phi/d\psi$) across the separatrix: E_r is driven negative inside the separatrix to prevent ion orbit loss, while

outside the separatrix the potential is positive due to the sheath potential established by parallel losses in the divertor. This produces a gradient scale-length in Φ that is comparable to the gyro-radius of high-energy ions. For example, the diameter of a deuterium ion with a perpendicular temperature around 4 keV has a gyro-orbit diameter approaching 1 cm or $\Delta\psi_N \approx 0.03$ at the outboard midplane. In other words, an ion experiences a non-uniform electric field during its gyromotion, resulting in a finite Larmor radius (FLR) correction to the $E \times B$ drift velocity. The FLR effect is approximated in the drift motion equations by averaging $\Phi(\psi)$ over the diameter of the gyro orbit. This approximate correction has the largest impact for the ion drift orbits around the separatrix ($0.98 < \psi_N < 1.02$). The implications of this correction will be discussed in more detail in a future section.

On the first time step of the simulation, the energy distributions are nearly Maxwellian everywhere in the simulation domain. Initially, a large number of ions are lost on collisionless orbits and the potential inside the separatrix becomes very negative, leading to an E_r well depth several times larger than what is expected from experiment. During the initial 2 ms of the simulation, the ion orbit loss rate decreases as the loss holes empty much faster than they are refilled, driving E_r more positive toward the experimentally observed value. The E_r profile is relatively constant after the first few milliseconds and evolves primarily in response to the convergence of the density profile to a steady-state solution.

Monte Carlo collisions are included in XGC0 by calculating the probability that a particle collides with any of the plasma species or a neutral atom. Probabilities are updated every time step based on the properties of the particle and the local properties of

the background plasma and neutral fluids. Background plasma and neutral properties used in the collision calculations are saved on a 2D spatial grid and updated every 100-200 time steps such that these properties evolve throughout the simulation. The background plasma is updated by querying the processors to accumulate the energy distributions of each species within an element of the grid. Moments of the distributions are taken to define the properties of a Maxwellian plasma background.

The code then uses the processors to launch millions of 3eV neutral deuterium particles from the wall locations where ions were lost. The number of ions lost to the limiter and the recycling rate sets the weight associated with each neutral particle. Neutral particles are followed until they ionize, charge-exchange or leave the simulation based on Monte Carlo collisions with the background plasma to establish the neutral deuterium properties (density, energy, flow) on the 2D grid. Deuterium ions will charge-exchange with the background deuterium neutrals, while charge exchange processes involving carbon ions are not included. Electron collisions with the background deuterium neutrals can result in an ionization event that adds a deuterium ion and electron to the simulation and subtracts the ionization energy away from the electron. Each deuterium ionization event also adds a carbon ion and six electrons, where the weight is scaled to reflect the estimated carbon neutral density. Thus, the code treats the carbon ions as a trace impurity where the sources and sinks due to ionization and charge-exchange are negligible.

XGC0 produces a flux-driven solution where the plasma profiles evolve to a solution consistent with the fluxes at the simulation boundaries. Particles, energy and parallel momentum are added to the simulation at the inner boundary by creating randomized

thermal particles and modifying the perpendicular and parallel energy of particles in the region $0.8 < \psi_N < 0.85$. The goal of this work is to use XGC0 to quantify the steady-state neoclassical and anomalous particle, energy and momentum transport rates that account for the core fluxes and the neutral sources and sinks in the H-mode pedestal. To that end, techniques were developed to quantitatively compare the XGC0 output to the measurements from the DIII-D charge-exchange spectroscopy (CER) and Thomson scattering diagnostics. The free-parameters in a simple 1D anomalous transport model in XGC0 are optimized to find good agreement between the synthetic diagnostic output generated by XGC0 and the experimental measurements.

A number of past studies with XGC0^{23,27} have demonstrated that additional (i.e. anomalous) transport is required in addition to the kinetic neoclassical transport to adequately describe the experimentally observed pedestals. The anomalous transport model chosen for this study is an energy-dependent random-walk model that perturbs the R, Z position of each guiding center:

$$\begin{aligned}\Delta R &= \left(\frac{D}{R} + \frac{dD}{d\psi} \frac{d\psi}{dR} \pm \sqrt{\frac{2D}{\Delta t}} \right) \Delta t + (\chi - D) V \frac{d\psi}{dR} \Delta t \\ \Delta Z &= \left(\frac{dD}{d\psi} \frac{d\psi}{dZ} \pm \sqrt{\frac{2D}{\Delta t}} \right) \Delta t + (\chi - D) V \frac{d\psi}{dZ} \Delta t \\ \text{where } V &= -\frac{2}{3} \left(\frac{K}{T} - \frac{3}{2} \right) \frac{dT/d\psi}{T}\end{aligned}\tag{1}$$

where ψ is the normalized poloidal flux coordinate, Δt is the time step, and R and Z give the spatial position of the particle. The \pm sign is defined randomly for each particle at a given ion time step. The average step size is the same for all species to reflect that the

average anomalous particle transport from small-scale fluctuations is ambipolar. The energy coefficient (χ) is independently defined for ions and electrons. When χ is greater than D , then high-energy particles ($K > T$) have a larger step size than low energy particles ($K < T$) where K is the ion energy and T is the average energy for a neighborhood of particles.

D and χ are input to the simulation as a 1D function versus ψ_N where the units are m^2/s at the outboard midplane. Figure 2a shows the 1D random-walk step-size profiles that are used for the calculations presented in this paper. These profiles represent the transport that was added to the neoclassical transport solution in order to best reproduce the experimental results. There are three regions with different anomalous transport properties. At the top of the pedestal ($\psi_N < 0.93$), the effective anomalous diffusion (D_{anom}) is $0.5 \text{ m}^2/\text{s}$, while the anomalous thermal diffusion ($\chi_{e,\text{anom}} = \chi_{i,\text{anom}}$) is $2 \text{ m}^2/\text{s}$. In the steep-gradient region ($0.95 < \psi_N < 0.99$), $D_{\text{anom}} = \chi_{\text{anom}} = 0.025 \text{ m}^2/\text{s}$ while $\chi_{e,\text{anom}}$ increases to $0.5 \text{ m}^2/\text{s}$ in the SOL ($\psi_N > 1$). Note that the random-walk model reduces to a fairly simple expression for the ions for $\psi_N > 0.95$ where $\chi = D$ and $dD/d\psi \sim 0$. The D and χ_e profiles are in good agreement with previous studies with interpretive and predictive H-mode transport models for the density and electron thermal transport^{2,28}.

The relationship between the three regions of anomalous transport and the pedestal shape is illustrated by the electron temperature (T_e) profile in Figure 2b, where the anomalous transport is reduced in the steep-gradient region of the pedestal ($0.94 < \psi_N < 1$). Random-walk motion determines the simulated electron thermal transport and the resulting T_e profile since neoclassical electron thermal transport is very small. Agreement between the simulated and measured electron temperature profile requires an

energy sink for electrons at the bottom of the pedestal and SOL ($\psi_N > 0.97$). The energy sink is tailored in the simulation using the free-parameters of a carbon line radiation model. Since the electron heat flux from the core, the anomalous transport model and line-radiation model have user-defined free-parameters, the electron temperature profile can always be brought into agreement with the data and the electron thermal transport rate is under-constrained in these simulations.

The version of XGC0 used in this study solves for the flux-surface-averaged potential and does not consider the potential variations along a field line. Therefore, the poloidal variations in the ion and electron charge densities are not equalized, especially in the SOL. In order to approximate the poloidally localized electron density at the position of the Thomson scattering measurements, the relative poloidal variation of the electron density is assumed to be the same as the ion charge density while the flux-surface-averaged value is unchanged:

$$n_e = \frac{n_D + 6n_C}{\langle n_D + 6n_C \rangle} \langle n_e \rangle$$

The difference between the assumed local electron density (n_e) and the flux-surface-averaged electron density ($\langle n_e \rangle$) is only significant in the SOL. In the XGC0 simulations with no E_{\parallel} , the electron density in the SOL is largest in the divertor where electrons are being sourced from neutral ionization. However, the ion density is peaked near the outboard midplane due to a large population of confined trapped ion orbits. In reality, a parallel electric field would develop with a positive potential near the outboard midplane to draw the electrons out of the divertor and equalize the local charge density throughout the SOL.

The density, temperature and velocity of fully-stripped carbon (C^{6+}) is measured using charge-exchange recombination (CER) spectroscopy on DIII-D²⁹. This diagnostic has viewing chords that intersect the neutral beam deposition region both vertically and tangentially at the outboard midplane. The poloidal flows and temperatures are computed using the tangential chord measurements to correct the vertical measurements for a small pickup of toroidal components due to the diagnostic viewing geometry. The toroidal and poloidal flows are corrected for atomic physics phenomenon³⁰ (these corrections were not included in the initial analysis of E_r presented in [9]). The XGC0 simulation is compared to the CER diagnostic measurement by taking moments of the computed C^{6+} distributions at the outboard midplane. The diamagnetic flow of each ion species is calculated in XGC0 using the gradient in the perpendicular pressure and added to $E \times B$ flow to include both the drift and fluid components of the measured flows. Future development of synthetic diagnostics for XGC0 will consider the line-integration of the viewing chords, which introduces some spatial smoothing of the measured profiles, especially for the vertical CER chords.

3. COMPUTATION OF NEOCLASSICAL AND ANOMALOUS TRANSPORT IN QH-MODE

The QH-mode discharge examined in this analysis had a plasma current (I_p) of 1.3 MA, an on-axis toroidal magnetic field of 2.0 T and 9.1 MW of counter- I_p neutral beam heating. The ion temperature at the top of the pedestal (~ 4 keV) is comparable to what is anticipated for burning plasma devices such as ITER, however the normalized pedestal Greenwald density and collisionality is considerably lower. The high-temperature, low-

density conditions enhance the kinetic effects on the pedestal structure and provide an opportunity to test kinetic simulations against experimental observations.

Figure 3 summarizes the agreement between the synthetic diagnostic profiles (red lines) with the measured density, temperature and flow profiles (black crosses). This agreement is achieved using a rigorous solution for the flux-driven kinetic neoclassical transport and a simple 1D anomalous transport model (Fig 2). Figure 4 summarizes the calculated moments of the ion distributions on closed flux surfaces. Each individual plot will be described in more detail during the discussion of the particle, energy and momentum transport that follows.

Particle transport and E_r

One significant result is that the XGC0 simulations capture the differences in the density pedestals for the three plasma species. Figure 3a shows the simulated electron density profile compared to the electron density measured with Thomson scattering. The electron density has little poloidal asymmetry inside the separatrix, but strong asymmetry in the SOL with a peak at the outboard midplane due to a significant population of trapped ions. This leads to a flattened (or even an increasing) density profile across the separatrix at the outboard edge of the plasma. The simulated ion densities (where $n_D = n_e - 6n_C$) at the outboard midplane are shown in Figure 3b. The deuterium density pedestal (dashed blue) is wider than the carbon density pedestal (solid red). This can also be appreciated when considering the flux surface averaged ion densities (Fig 4a) and their gradients (Fig 4b). The peak density gradient for carbon is inside the separatrix, while the maximum deuterium density gradient is near the separatrix. This leads to a non-monotonic effective ion charge (Z_{eff}) across the pedestal (decreasing from three at the top

of the pedestal to about 2 at the separatrix). The radial variation in $\langle Z_{\text{eff}} \rangle$ must be considered when computing the equilibrium and stability of H-mode pedestals.

The difference between the density profiles is understood when considering the anomalous and neoclassical particle transport mechanisms. Neoclassical electron particle transport is small, and thus the electron particle transport in the pedestal is typically equal to the anomalous transport rate. However, the ion species have neoclassical particle fluxes that are significant, but typically offset. In this particular case, the neoclassical deuterium flux is outward, while the neoclassical carbon flux is inward. These offsetting fluxes result in ion density pedestals that become steeper at the outboard midplane with increasing Z due to the orbit squeezing in the region of strong negative E_r . In the QH-mode discharges with a deep E_r well, the simulated in-out asymmetry of the carbon density within the pedestal is large and peaked on the high-field side (similar to the observed impurity density asymmetry in³¹). Furthermore, the neoclassical pinch of the carbon ions provides a mechanism for the C^{6+} density profile to exist with only neutral recycling as a source.

Figure 5 shows the particle ionization source rates and the different components of the radial particle flux. The core particle flux from the neutral beams is 10^{21} deuterium and electron particles per second (160 Amps). The recycling rate at the limiter for deuterium and carbon is set to 0.9 and 1.0, respectively, in order to maintain a constant particle inventory in the simulation. The resulting particle source from ionization is shown in Figure 5a. The total electron particle flow (Fig 5b) is solely due to anomalous processes at the top of pedestal ($\psi_N < 0.94$), whereas the neoclassical transport can

contribute around half of the net particle transport in the steep-gradient region ($0.94 < \psi_N < 1$).

The finite neoclassical electron flux in the steep-gradient region is a consequence of the large negative E_r that widens the electron radial orbit excursions across the steep density gradient. It is important to consider that the electron mass was enhanced by about 36 in the simulations, resulting in orbit excursions that are a factor of six too large. A new calculation is being performed with a mass enhancement of 4 (at larger computational expense) to investigate the dependence of the computed neoclassical electron particle flux on its mass. As expected, the preliminary results indicate the factor of nine reduction in the electron mass reduces the neoclassical particle flux by a factor of three. As a consequence the anomalous transport rate in the steep-gradient region is doubled ($D_{\text{anom}} = 0.05 \text{ m}^2/\text{s}$) to maintain a good match to the experimental data. Therefore, while the results from the presented simulation suggest neoclassical particle transport can be as large as the anomalous transport rate in the steep-gradient region, it is more likely the case that the electron transport is completely due to the anomalous processes.

The random-walk model is designed to be ambipolar and thus the anomalous electron current is equal to the sum of the anomalous ion currents (blue solid lines in Fig 5b-c). XGC0 solves for the E_r that balances the electron and ion neoclassical currents (black solid lines). The self-consistent E_r that maintains ambipolar neoclassical transport in XGC0 is shown in Fig. 6 (red line). The electron motions respond to this field, while the ion guiding centers experience a gyro-averaged E_r with reduced radial gradients. The dashed red in line if Fig. 6 is the average $v_{E \times B} \times B$ for the carbon ions at the outboard midplane, representing the E_r inferred from carbon force balance. This is in good

agreement with the E_r inferred from fits to the CER profiles and assuming C^{6+} force balance (black line). The FLR correction becomes important for achieving a good match between the simulation and experiment at the bottom of the pedestal ($0.98 < \psi_N < 1$), where E_r becomes more positive towards the separatrix. A consequence of the FLR effect is that the gyro-averaged E_r , which is reflected in the measured ion force balance, will approach the true radial electric field with a large gradient across the separatrix as the larmor radius ($\sim \sqrt{T_{\perp} M_i} / ZB$) becomes smaller.

The FLR effect is important in computing the kinetic transport of ions, especially deuterium ions with large magnetic moments (μ), around the separatrix. These high-energy ions can have a guiding center inside the separatrix, yet partially sample the positive E_r outside the separatrix. The gyro-radius is large (\sim cm) at the outboard midplane separatrix in these simulations due to ion perpendicular temperatures (Fig 3c, where $T_{\perp} \sim T_{\theta}$) that is much larger than the electron and ion parallel temperatures. Consequently, ions with a large gyro-orbit will have a more positive gyro-averaged E_r inside the separatrix and a larger outward neoclassical flux than ions with smaller gyro-orbits. In the frame of the net radial flow of deuterium ions, this appears as a pinch of cold ions that can balance the enhanced outward flow of high-energy ions.

Energy transport

The C^{6+} temperature profiles measured by the orthogonal CER views at the outboard midplane are different in the steep-gradient region and SOL of high-temperature, low-collisionality QH-mode pedestals on DIII-D and the XGC0 simulation reproduces both T_{θ} (Fig 3c) and T_{ϕ} (Fig 3d) in the steep-gradient region. The simulation is also in qualitative agreement with the observed increase in the C^{6+} temperature in the SOL at the

outboard midplane due to the population of high-energy trapped particles that originate from the top of the pedestal becoming the dominate density source in the far SOL³². The temperature anisotropy ($T_{\parallel} \neq T_{\perp}$) at the outboard midplane for the two ion species is compared in Fig 7, where the anisotropy is larger for the D⁺ ions compared to the C⁶⁺ impurity.

The QH-mode discharge was heated with 9.1 MW of counter-I_p neutral beam injection and about 1 MW of ohmic heating. The corresponding core heat fluxes used for the XGC0 simulations are 6.5 MW of deuterium heating, 0.5MW of carbon heating and 1 MW of electron heating. The majority of the deuterium heat flux is conductive, with small convective (0.6 MW) and rotational heating (0.5 MW) contributions. The carbon heating is primarily from rotational heating. The large difference in heating between deuterium and carbon is due to the difference in the particle densities as illustrated in Fig 4c where the average energy for each ion species ($\langle K \rangle = \langle (K_{\parallel} + K_{\perp}) / (n Vol) \rangle$) is fairly well matched.

Figure 8a shows the computed sources and sinks of energy for ions, such as collisional exchange, charge exchange with neutrals and ionization. Charge exchange loss to neutrals is computed only for deuterium (yellow line) and is the largest sink of ion energy in the calculations. The energy source from ionization (purple) and the collisional exchange losses to the electrons (green) is the total for both ion species. Figures 8b-c show the contributions of the anomalous and neoclassical transport to the flux-surface averaged ion heat flow through the pedestal. The ion heat flow is predominately anomalous at the top of the pedestal ($\psi_N < 0.94$), and predominately neoclassical in the steep-gradient region, especially for deuterium. About 6 MW of heat flows through the

pedestal via the ions, with about 3MW lost to collisions with electrons and neutrals and the remaining 3MW transported to the SOL by deuterium ions.

Momentum transport

The toroidal and poloidal flows at the outboard midplane are shown in Fig. 3e-f. These flows are the sum of the $E \times B$ flow directly computed in XGC0 and the diamagnetic flow estimated using the gradient in the perpendicular pressure. Both components of the simulated C^{6+} flow (red lines) are in good agreement with the measurements for $\psi_N < 1$. The corresponding D^+ flows (dashed blue lines) are calculated to be significantly different at the outboard midplane, especially in the toroidal direction where the flow is about 100km/s offset from the carbon in the co- I_p direction. The toroidal flow at the top of the pedestal is in the counter- I_p direction due to the applied torque at the inner boundary and reverses direction near the separatrix.

Collisions keep the average ion energy (Fig 4c) fairly well matched between carbon and deuterium; however the parallel flows (Fig 4e) can be quite different. The difference in the parallel flows is appreciated when examining the energy distributions of the ions. Figure 9 shows the computed energy distributions for deuterium and carbon at the outboard midplane at $\psi_N = 0.84$. The orbit excursion of deuterium ions (Fig 9a) is six times larger than carbon (Fig 9b), amplifying the kinetic effects and leading to a velocity distribution that is highly non-Maxwellian. The important feature is the large hole in the counter- I_p velocity space for deuterium due to ion orbit loss.

The loss hole extends to its lowest energy for trapped ions near the trapped-passing boundary that have reflection points close to the inboard midplane. One consequence of this loss hole is that the tail of the distribution is skewed toward co- I_p and the moment of

the parallel velocity distribution (red lines) is more co- I_p than the bulk ions (blue). On the other hand, the carbon ions have less distortion of the high-energy tail and the Gaussian fit to the parallel velocity distribution is centered on the bulk flow. The net result is an intrinsic torque in the co- I_p direction at the outboard midplane that is species dependent. This drives a separation in parallel flows where the deuterium flow is more co- I_p than carbon. The direction of the intrinsic torque is reversed at the inboard midplane (counter- I_p); however it is smaller in magnitude due to toroidal effects. Thus, the net torque on each flux surface from kinetic effects near the separatrix is in the co- I_p direction. In this particular case, the core plasma is rotating in the counter- I_p direction due to the external torque from the neutral beam injection, while the intrinsic torque in the pedestal reverses the flow.

4. IMPLICATION OF KINETIC NEOCLASSICAL TRANSPORT IN H-MODE PEDESTAL TRANSPORT

This kinetic neoclassical calculation indicates that a small number of high-energy ions in the tail of the thermal energy distribution transport most of the energy across the H-mode pedestal, while anomalous processes transport the colder bulk ions and account for at least half of the particle flux with relatively less impact on the energy flux. Separation of particle and energy transport processes across the pedestal is often seen in ELM-free tokamak regimes, including QH-mode, where a 3D edge perturbation from a mode increases the particle flux through the pedestal with minimal impact on the energy transport. This is consistent with the result that particle transport, and thus the density pedestal, are more affected by anomalous transport than energy transport and the corresponding temperature profile. The separation of energy and particle transport

processes can also play a role in the evolution of the H-mode pedestal following the L-H transition or an ELM where the temperature and density pedestals will often evolve on different timescales.

The energy distributions of the ions in the pedestal are computed to be non-Maxwellian in the simulated high temperature, low collisionality H-mode pedestal. One implication is that the ion temperature is anisotropic and species dependent, which must be considered when interpreting edge measurements for pedestal equilibrium and stability calculations. Another implication is that there is a source of intrinsic co- I_p torque at the plasma edge. Ion orbit loss has been proposed in a number of studies as the source of the intrinsic co- I_p edge torque that is seen on all tokamaks^{33,34}. These calculations are among the first to quantitatively demonstrate that kinetic neoclassical effects can reproduce this torque. Recent work with XGC1 demonstrated that ITG-like turbulence at the top of the pedestal is necessary for pinching the edge torque inwards toward the core on DIII-D³⁵. The intrinsic torque is important for future devices, such as ITER, where it is predicted to be comparable to the externally applied torque from neutral beams.

Perhaps the most significant implication of kinetic neoclassical transport is that ion orbit loss plays an important role in establishing the structure of the radial electric field at the tokamak edge. The work presented in this paper provides a quantitative investigation of a long-standing theory that the edge E_r is the unique solution (i.e. ion root) that maintains ambipolar neoclassical transport and that ion orbit loss is the primary non-ambipolar source that drives the neoclassical solution. The agreement between the E_r inferred from the experimental measurements and the E_r computed using XGC0 is promising within the caveats discussed earlier concerning the enhanced electron mass

and approximate FLR correction. At a minimum, the simulation indicates that the particle transport from ion orbit loss when E_r is near the experimental value is at a reasonable level compared to the neutral beam and neutral recycling particle sources.

A widely accepted theory is that the equilibrium $E \times B$ shear at the edge stabilizes the edge turbulence and sustains the H-mode transport barrier. The shear generated by the kinetic neoclassical solution for E_r depends strongly on the ion temperature and the magnetic geometry. As a consequence, the edge ion temperature required to access H-mode is a function of the magnetic geometry. A previous study on NSTX established that the edge ion temperature required for H-mode increased as the triangularity of the plasma increased, while it was independent of the neutral fueling conditions and the edge heat flux³⁶.

The relationship between T_i and E_r also is important in the positive feedback loop that drives the bifurcation in the transport between L- and H-mode. The confinement of the tail deuterium ions that determine the ion heat flux through the pedestal improves with more negative E_r . This will lead to an increased edge ion temperature at the edge, requiring E_r to become more negative to suppress ion orbit loss. This increases the width of the high-shear region and is a viable mechanism to describe the expansion of the pedestal width following the L-H transition or an ELM crash.

5. CONCLUSIONS AND FUTURE WORK

The fusion power gain of future burning plasma devices of a fixed geometry, such as ITER, is predicted to increase with increasing pedestal pressure height³⁷. Peeling-ballooning stability theory predicts that the maximum stable pedestal pressure increases with reduced pedestal pressure gradients. Therefore, predicting and optimizing the pedestal for a burning plasma regime relies on understanding what mechanisms determine the total particle and energy transport. Optimizing fusion reactor designs will also require an understanding of the intrinsic momentum sources, sinks and transport in the H-mode pedestal. Both the perpendicular and parallel flows play significant roles in the self-organization of the pedestal through the flow shear suppression of turbulence, stability of the pedestal to a variety of modes, and the penetration of non-axisymmetric fields. It is also important to understand the processes that control the transport of impurity ions through the pedestal since the performance of fusion reactors is dependent on flushing impurities, including helium ash, from the confined plasma and limiting the influx of impurities introduced at the plasma boundary from wall materials and divertor impurity seeding.

Edge transport models capable of quantitative flux-driven predictions of the self-organization of the H-mode pedestal must consider the non-linear multi-scale coupling of the plasma and atomic physics without any limitations on the energy distributions of the particles. The XGC0 simulation presented in this article presents the first calculation of axisymmetric 5D drift-kinetic transport with kinetic deuterium, electrons and fully-stripped carbon in a realistic magnetic geometry with a self-consistent solution for E_r on closed and open magnetic field lines and neutral wall recycling. A simple ad-hoc

turbulent transport model was used to obtain a quantitative match between synthetic diagnostics in the simulation and experimental measurements, providing an interpretative tool for determining the balance between neoclassical and anomalous transport processes. The XGC0 simulations are performed for a QH-mode discharge on DIII-D. This unique regime achieves reactor-relevant pedestal parameters with steady-state transport maintained by an edge harmonic oscillation. The steady-state transport provides an ideal environment for long integration, high spatial resolution measurements that provide detailed profiles with low signal-to-noise.

Three important conclusions are drawn from the interpretive analysis of QH-mode transport using XGC0. The first is that the ion thermal transport is close to the neoclassical level in the steep gradient region. Most of the energy in the QH-mode regime is carried through the transport barrier by tail deuterium ions. The second is that a number of experimental observations, such as temperature anisotropy, large SOL temperatures, poloidal asymmetries, and intrinsic flows are quantitatively described by considering the kinetic transport and resulting distortion of the energy distribution. These effects are not captured by fluid or standard analytic neoclassical calculations that assume the energy distribution is close to Maxwellian, yet these effects must be considered in the interpretation of edge diagnostics and understanding the transport mechanisms. Finally, the results illustrate that axisymmetric kinetic neoclassical transport can capture the mechanisms important for the self-consistent edge neoclassical radial electric in the H-mode pedestal. The characteristic reversal of E_r across the separatrix is determined by the ion orbit loss inside the separatrix and the wall sheath outside the separatrix.

The ability of the simulation to reproduce the density, temperature and flow profiles is encouraging, but a number of advances are needed for a fully predictive model. Obviously, the ad-hoc anomalous transport model will need to be replaced by either an analytic model (where D and χ are estimated from the local gradients and the $E \times B$ shear) or a direct calculation with a code like XGC1. Furthermore, the neutral recycling and impurity radiation models will need to be more complete. For example, the model will need to consider all the molecular and charge states of the ions and the energy dependent sputtering of neutrals from the wall. The state-of-the-art calculations that include the necessary atomic and solid-state physics have been demonstrated in other edge transport calculations, but are in the process of being incorporated into XGC0.

The impact of a number of assumptions used to speed up the calculations will be investigated in the near future. Work is on-going to complete a simulation with reduced electron mass to investigate the impact on the neoclassical electron particle transport. Furthermore, the code calculations could be expanded to include the non-axisymmetric magnetic perturbations expected from the EHO mode on the neoclassical transport. Also, the neoclassical solution in XGC0 is not complete since it does not include the modification of the drift orbits from toroidal or poloidal electric fields. This omission has the largest impact on the neoclassical radial flux of the impurity ion and the poloidal distribution of the electron density. The upgrade to XGC0, called XGCa, will include all components of the electric field, which should provide a more accurate model for the impurity transport and the flows within the SOL. XGCa will also include a more complete correction for FLR effects that are important near the separatrix.

The full-f kinetic neoclassical transport calculation presented in this article represents a major step forward in the development of a quantitative model that could be used to design, control and optimize the H-mode pedestal in future burning-plasma devices. The combination of the detailed pedestal measurements with the large-scale kinetic solution demonstrates that the field is now capable of leveraging the recent advances in diagnostics and computation power toward meeting the critical challenge of measuring and simulating the self-organization of the H-mode pedestal.

Acknowledgments

This work was supported by the U.S. Department of Energy under DE-AC02-09CH11466 and DE-FG02-95ER54309. This research used resources of the National Energy Research Scientific Computing Center, which is supported by the U.S. Department of Energy under DE-AC02-05CH11231. The authors gratefully acknowledge the contributions of the teams at the DIII-D National Fusion Facility and the Edge Physics Simulation Project. In particular, D. Stotler and R. Hager for continuous support for the XGC0 code. D. Battaglia is grateful to R. Groebner, J. Canik, R. Maingi, R. Nazikian, S. Kaye, and co-authors for guidance during this work.

References

- [1] Wagner, F. (2007). A quarter-century of H-mode studies. *Plasma Physics and Controlled Fusion*, 49(12B), B1–B33. doi:10.1088/0741-3335/49/12B/S01
- [2] Callen, J. D., Groebner, R. J., Osborne, T. H., Canik, J. M., Owen, L. W., Pankin, a. Y., Rafiq, T., et al. (2010). Analysis of pedestal plasma transport. *Nuclear Fusion*, 50(6), 064004. doi:10.1088/0029-5515/50/6/064004
- [3] Burrell, K. (1997). Effects of $E \times B$ velocity shear and magnetic shear on turbulence and transport in magnetic confinement devices. *Physics of Plasmas*, 4(5), 1499–1518.
- [4] Terry, P. (2000). Suppression of turbulence and transport by sheared flow. *Reviews of Modern Physics*, 72(1), 109–165. doi:10.1103/RevModPhys.72.109
- [5] Snyder, P. B., Groebner, R. J., Leonard, a. W., Osborne, T. H., & Wilson, H. R. (2009). Development and validation of a predictive model for the pedestal height. *Physics of Plasmas*, 16(5), 056118. doi:10.1063/1.3122146
- [6] Burrell, K. H., West, W. P., Doyle, E. J., Austin, M. E., Casper, T. a., Gohil, P., Greenfield, C. M., et al. (2005). Advances in understanding quiescent H-mode plasmas in DIII-D. *Physics of Plasmas*, 12(5), 056121. doi:10.1063/1.1894745
- [7] Snyder, P. ., Burrell, K. ., Wilson, H. ., Chu, M. ., Fenstermacher, M. ., Leonard, a. ., Moyer, R. ., et al. (2007). Stability and dynamics of the edge pedestal in the low collisionality regime: physics mechanisms for steady-state ELM-free operation. *Nuclear Fusion*, 47(8), 961–968. doi:10.1088/0029-5515/47/8/030
- [8] Burrell, K., Osborne, T., Snyder, P., West, W., Fenstermacher, M., Groebner, R., Gohil, P., et al. (2009). Quiescent H-Mode Plasmas with Strong Edge Rotation in

- the Cocurrent Direction. *Physical Review Letters*, 102(15), 155003.
doi:10.1103/PhysRevLett.102.155003
- [9] Burrell, K. H., West, W. P., Doyle, E. J., Austin, M. E., deGrassie, J. S., Gohil, P., Greenfield, C. M., et al. (2004). Edge radial electric field structure in quiescent H-mode plasmas in the DIII-D tokamak. *Plasma Physics and Controlled Fusion*, 46(5A), A165–A178. doi:10.1088/0741-3335/46/5A/018
- [10] Connor, J. ., Fukuda, T., Garbet, X., Gormezano, C., Mukhovatov, V., Wakatani, M., Group, the I. D., et al. (2004). A review of internal transport barrier physics for steady-state operation of tokamaks. *Nuclear Fusion*, 44(4), R1–R49. doi:10.1088/0029-5515/44/4/R01
- [11] Shaing, K., & Jr, E. C. (1989). Bifurcation Theory of Poloidal Rotation in Tokamaks: A Model for the L-H Transition. *Physical Review Letters*, 63(21), 2326
- [12] Groebner, R., Burrell, K., & Seraydarian, R. (1990). Role of edge electric field and poloidal rotation in the LH transition. *Physical review letters*, 64(25), 3015–3018.
- [13] Heikkinen, J., Kiviniemi, T., & Peeters, A. (2000). Neoclassical radial current balance in tokamaks and transition to the H mode. *Physical review letters*, 84(3), 487–90.
- [14] Chang, C. S., Kue, S., & Weitzner, H. (2002). X-transport: A baseline nonambipolar transport in a diverted tokamak plasma edge. *Physics of Plasmas*, 9(9), 3884. doi:10.1063/1.1490348
- [15] Stacey, W. M. (2013). Effect of ion orbit loss on the structure in the H-mode tokamak edge pedestal profiles of rotation velocity, radial electric field, density, and temperature. *Physics of Plasmas*, 20(9), 092508. doi:10.1063/1.4820954

- [16] Chankin, A., & McCracken, G. (1993). Loss ion orbits at the tokamak edge. *Nuclear fusion*, 33(10), 1459.
- [17] Miyamoto, K. (1996). Direct ion orbit loss near the plasma edge of a divertor tokamak in the presence of a radial electric field. *Nuclear fusion*, 927.
- [18] Ku, S., Baek, H., & Chang, C. S. (2004). Property of an X-point generated velocity-space hole in a diverted tokamak plasma edge. *Physics of Plasmas*, 11(12), 5626. doi:10.1063/1.1812273
- [19] deGrassie, J. S., Müller, S. H., & Boedo, J. a. (2012). Plasma flow due to a loss-cone distribution centred around the outboard edge in DIII-D. *Nuclear Fusion*, 52(1), 013010. doi:10.1088/0029-5515/52/1/013010
- [20] Chang, C. S., & Ku, S. (2006). Particle Simulation of Neoclassical Transport in the Plasma Edge. *Contributions to Plasma Physics*, 46(7-9), 496–503. doi:10.1002/ctpp.200610036
- [21] Xu, X. ., Xiong, Z., Dorr, M. ., Hittinger, J. ., Bodi, K., Candy, J., Cohen, B. ., et al. (2007). Edge gyrokinetic theory and continuum simulations. *Nuclear Fusion*, 47(8), 809–816. doi:10.1088/0029-5515/47/8/011
- [22] Dorf, M. a., Cohen, R. H., Dorr, M., Rognlien, T., Hittinger, J., Compton, J., Colella, P., et al. (2013). Simulation of neoclassical transport with the continuum gyrokinetic code COGENT. *Physics of Plasmas*, 20(1), 012513. doi:10.1063/1.4776712
- [23] Chang, C. S., Ku, S., & Weitzner, H. (2004). Numerical study of neoclassical plasma pedestal in a tokamak geometry. *Physics of Plasmas*, 11(5), 2649. doi:10.1063/1.1707024

- [24] Chang, C. S., Ku, S., Diamond, P. H., Lin, Z., Parker, S., Hahm, T. S., & Samatova, N. (2009). Compressed ion temperature gradient turbulence in diverted tokamak edge. *Physics of Plasmas*, *16*(5), 056108. doi:10.1063/1.3099329
- [25] Ku, S., Chang, C. S., & Diamond, P. H. (2009). Full-f gyrokinetic particle simulation of centrally heated global ITG turbulence from magnetic axis to edge pedestal top in a realistic tokamak geometry. *Nuclear Fusion*, *49*(11), 115021. doi:10.1088/0029-5515/49/11/115021
- [26] <http://epsi.pppl.gov/>
- [27] Pankin, a. Y., Kruger, S. E., Groebner, R. J., Hakim, a., Kritz, a. H., & Rafiq, T. (2013). Validation of transport models using additive flux minimization technique. *Physics of Plasmas*, *20*(10), 102501. doi:10.1063/1.4823701
- [28] Callen, J., Canik, J., & Smith, S. (2012). Pedestal Structure Model. *Physical Review Letters*, *108*(24), 245003. doi:10.1103/PhysRevLett.108.245003
- [29] Thomas, D. M., Mckee, G. R., Burrell, K. H., Levinton, F., Foley, E. L., & Fisher, R. K. (2008). CHAPTER 6 ACTIVE SPECTROSCOPY. *Fusion science and technology*, *53*, 487.
- [30] Solomon, W. M., Burrell, K. H., Gohil, P., Groebner, R. J., & Baylor, L. R. (2004). Extraction of poloidal velocity from charge exchange recombination spectroscopy measurements. *Review of Scientific Instruments*, *75*(10), 3481. doi:10.1063/1.1790042
- [31] Churchill, R. M., Lipschultz, B., & Theiler, C. (2013). In-out impurity density asymmetry in the pedestal region of Alcator C-Mod. *Nuclear Fusion*, *53*(12), 122002. doi:10.1088/0029-5515/53/12/122002

- [32] Lasnier, C., & Burrell, K. (2003). Scrape-off layer features of the QH-mode. *Journal of Nuclear Materials*, 313-6(March), 904–8.
- [33] deGrassie, J. S., Groebner, R. J., Burrell, K. H., & Solomon, W. M. (2009). Intrinsic toroidal velocity near the edge of DIII-D H-mode plasmas. *Nuclear Fusion*, 49(8), 085020. doi:10.1088/0029-5515/49/8/085020
- [34] Solomon, W. M., Burrell, K. H., deGrassie, J. S., Boedo, J. a., Garofalo, a. M., Moyer, R. a., Muller, S. H., et al. (2011). Characterization of intrinsic rotation drive on DIII-D. *Nuclear Fusion*, 51(7), 073010. doi:10.1088/0029-5515/51/7/073010
- [35] Seo, J., Chang, C.S., Ku, S., Kwon, J.M., Yoon, E.S., GP8.00008: Detailed study of spontaneous rotation generation in diverted H-mode plasma using the full-f gyrokinetic code XGC1. 55th Annual Meeting of the APS Division of Plasma Physics, 2013 Bulletin of the Americal Physical Society, 58(16)
- [36] Battaglia, D. J., Chang, C. S., Kaye, S. M., Kim, K., Ku, S., Maingi, R., Bell, R. E., et al. (2013). Dependence of the L–H transition on X-point geometry and divertor recycling on NSTX. *Nuclear Fusion*, 53(11), 113032. doi:10.1088/0029-5515/53/11/113032
- [37] Kinsey, J., Bateman, G., & Onjun, T. (2003). Burning plasma projections using drift-wave transport models and scalings for the H-mode pedestal. *Nuclear Fusion*, 43, 1845–54. Retrieved from <http://iopscience.iop.org/0029-5515/43/12/027>

Figure Captions

FIG 1: Magnetic equilibrium used for XGC0 simulations. Contour separation is $\Delta\psi_N = 0.1$. B_ϕ is into the page (ion ∇B drift is down) and I_p is out of the page.

FIG 2: (a) Coefficients for anomalous transport model used in the XGC0 simulations (b) Simulated electron temperature profile (solid red) compared to measurement (black crosses). Vertical dotted lines separate three transport regions: top of pedestal, steep-gradient region and scrape-off layer.

FIG 3: (a) XGC0 synthetic diagnostic output for n_e (solid red) at Thomson scattering location compared to measurements (black crosses). (b-f) Simulated profiles for C^{6+} (solid red) and D^+ (dashed blue) at outboard midplane compared to CER measurement of C^{6+} (black crosses) for: (b) density, (c) poloidally viewed ion temperature, (d) toroidally viewed ion temperature, (e) poloidal velocity and (f) toroidal velocity. Vertical dashed lines indicate the transition in the anomalous coefficients ($\psi_N = 0.94$) and the separatrix.

FIG 4: Flux-surface average quantities and their gradients for C^{6+} (solid red) and D^+ (dashed blue): (a-b) ion density, (c-d) total ion energy, and (e-f) parallel velocity. Vertical dashed line indicates the transition in the anomalous coefficients ($\psi_N = 0.94$).

FIG 5: (a) Charge source rate from D^+ (purple) and C^{6+} (green) ionization. (b) Neoclassical (solid black) and anomalous (solid blue) contributions to the total (dash-dot black) particle flux of electrons. Total charge flow is nearly equal to the particle source rate times the particle charge since $dn/dt \approx 0$. The 10^{21} particles/s for deuterium and

electrons sourced from the core equates to 160 Amps of radial current. (c) Ion charge flux for deuterium (solid black, blue) and carbon (dashed black, blue).

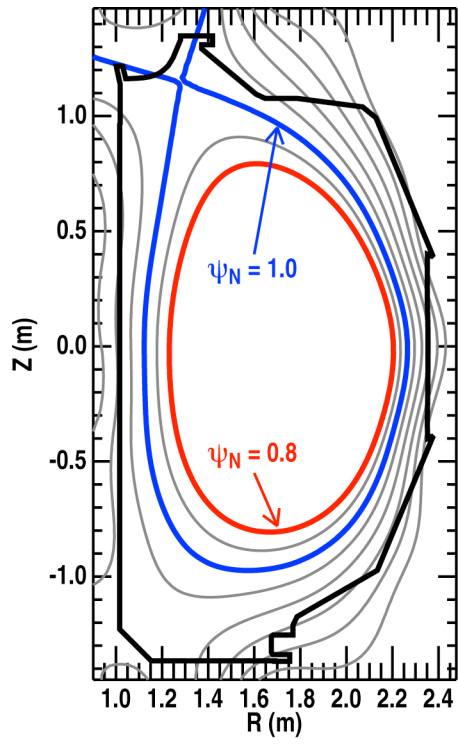
FIG 6: Self-consistent E_r at the outboard midplane computed using XGC0 (solid red) compared to the E_r inferred from the measured C^{6+} profiles using force balance (solid black). Dashed red line is the E_r calculated from force balance with the gyro-averaged E_r in XGC0.

FIG 7: Perpendicular (solid) and parallel (dashed) temperatures at outboard midplane for deuterium (blue) and carbon (red).

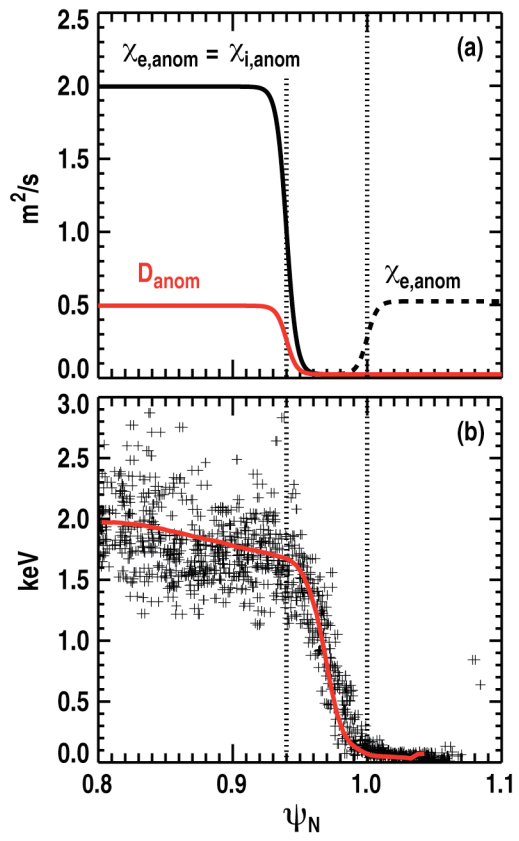
FIG 8: (a) Ion energy sources and sinks. (b) Neoclassical (solid black) and anomalous (solid blue) contributions to the total (dash-dot black) heat flux for deuterium and (c) carbon.

FIG 9: D^+ and C^{6+} velocity distributions at top of pedestal. The top panels show computed contours of particle weights (black lines) in 2D velocity space for (a) D^+ and (b) C^{6+} . Dashed blue lines show the v/v_{th} contours for a shifted Maxwellian centered on the average flow of the cold bulk ions (vertical blue line). Solid green lines are the estimated trapped-passing boundaries [19, eq. A.6]. Bottom panels are the $v_{||}/v_{th}$ distributions for (c) D^+ and (d) C^{6+} . Solid red line is a Gaussian fit (vertical red dash is Gaussian center).

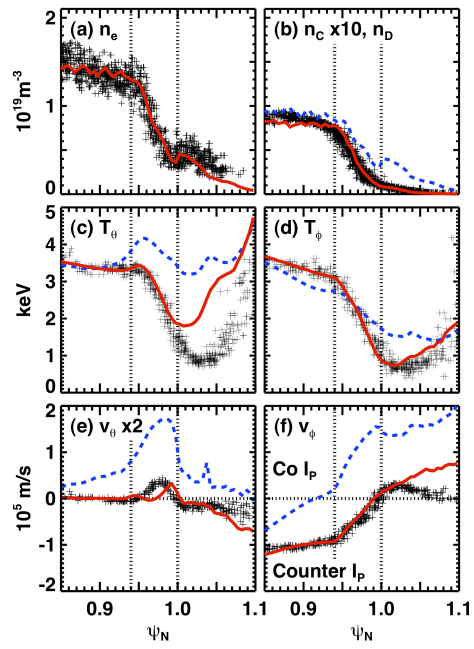
List of Figures



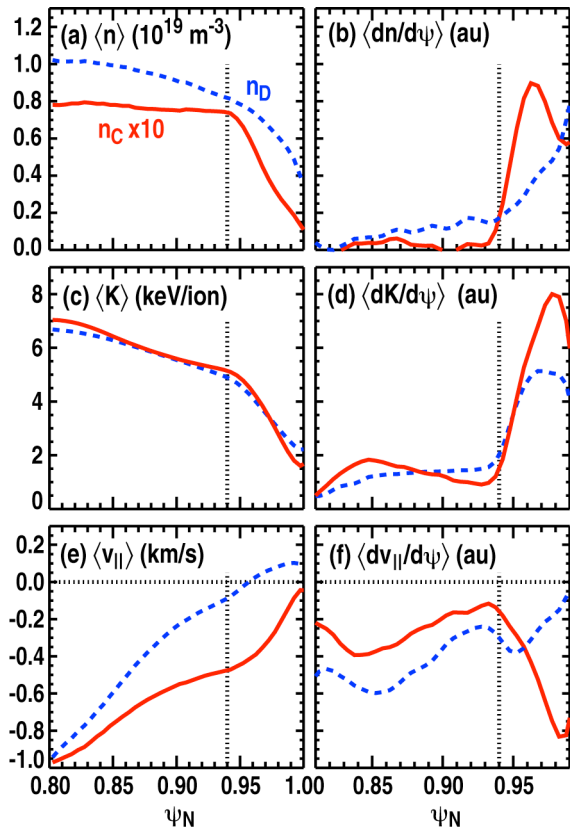
D.J. Battaglia Fig. 1



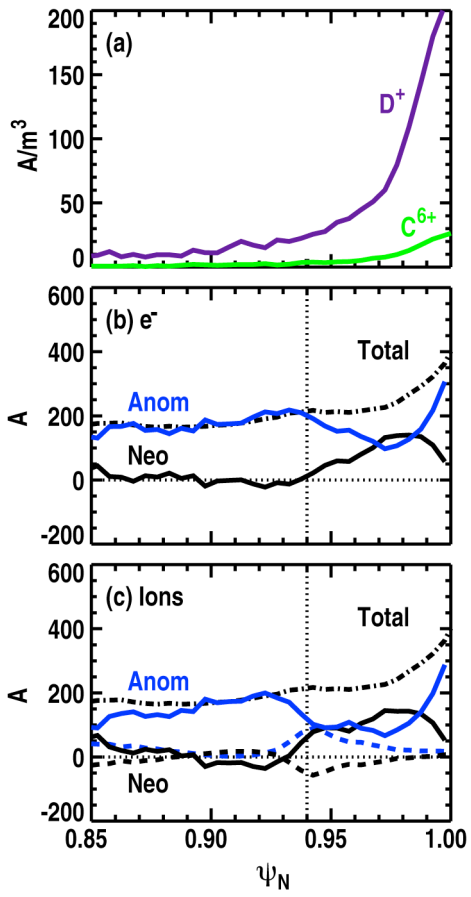
D.J. Battaglia Fig. 2



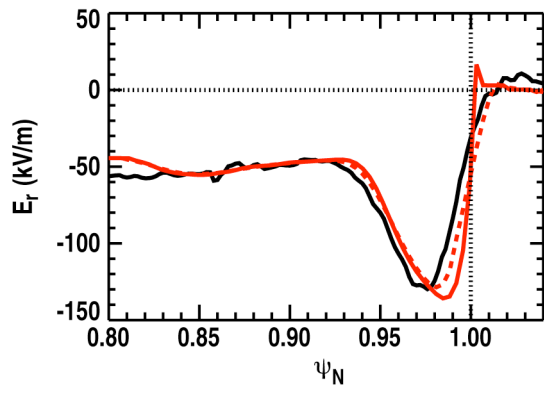
D.J. Battaglia Fig 3



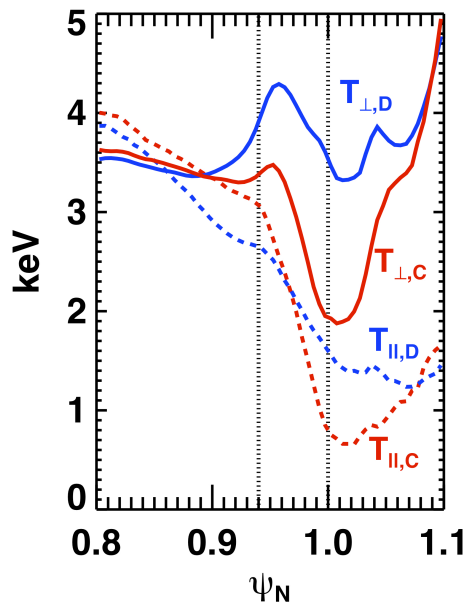
D.J. Battaglia Fig. 4



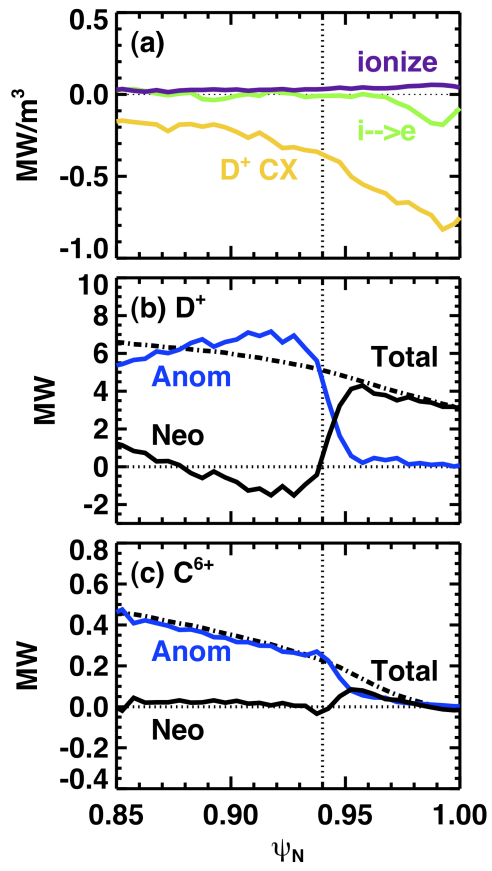
D.J. Battaglia Fig. 5



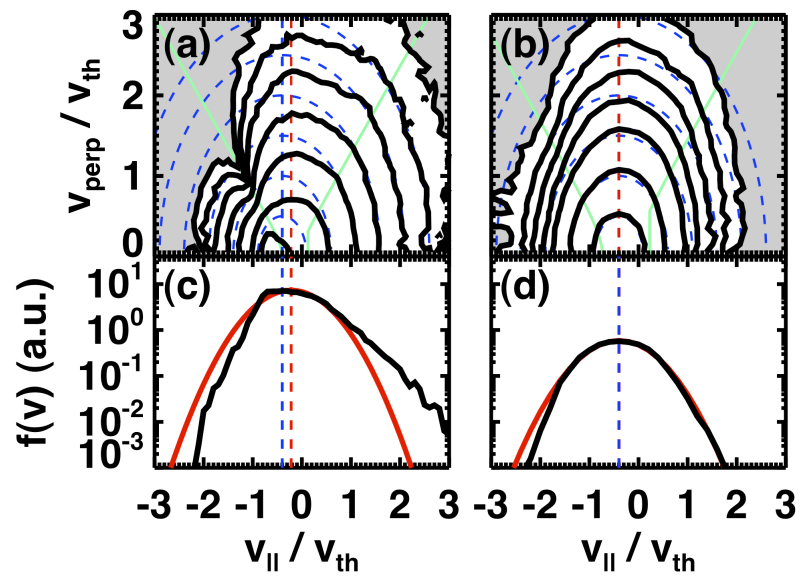
D.J. Battaglia Fig. 6



D.J. Battaglia Fig. 7



D.J. Battaglia Fig. 8.



D.J. Battaglia Fig. 9

The Princeton Plasma Physics Laboratory is operated
by Princeton University under contract
with the U.S. Department of Energy.

Information Services
Princeton Plasma Physics Laboratory
P.O. Box 451
Princeton, NJ 08543

Phone: 609-243-2245
Fax: 609-243-2751
e-mail: pppl_info@pppl.gov
Internet Address: <http://www.pppl.gov>